COMPUTER MODELING

Energy-level alignment at organic heterointerfaces

Martin Oehzelt,[1,2]* Kouki Akaike,[2†] Norbert Koch,[1,2] Georg Heimel[2]

10.1126/sciadv.1501127

Today's champion organic (opto-)electronic devices comprise an ever-increasing number of different organic-semiconductor layers. The functionality of these complex heterostructures largely derives from the relative alignment of the frontier molecular-orbital energies in each layer with respect to those in all others. Despite the technological relevance of the energy-level alignment at organic heterointerfaces, and despite continued scientific interest, a reliable model that can quantitatively predict the full range of phenomena observed at such interfaces is notably absent. We identify the limitations of previous attempts to formulate such a model and highlight inconsistencies in the interpretation of the experimental data they were based on. We then develop a theoretical framework, which we demonstrate to accurately reproduce experiment. Applying this theory, a comprehensive overview of all possible energy-level alignment scenarios that can be encountered at organic heterojunctions is finally given. These results will help focus future efforts on developing functional organic interfaces for superior device performance.

INTRODUCTION

Tremendous research efforts on the materials science of organic (opto-)electronics have led to considerable progress over the past decades. Highly efficient organic light-emitting diodes (OLEDs) have entered the market and are on their way to dominate display technology. Also, organic photovoltaic cells (OPVCs) offer unique advantages over their inorganic counterparts. In particular, the operating time needed to recover the energy invested in making an OPVC, that is, its energy payback time, can potentially be reduced to days (*1*, *2*), whereas it is on the order of years for conventional technology (*3*). Since the discovery and first studies of organic semiconductors in the late 1950s (*4*, *5*), subsequent increases in device performance frequently correlated with increases in their complexity. Early devices first consisted of only one (*6*–*8*) or two organic layers (*9*–*11*) sandwiched between conducting electrodes, whereas modern device architectures often exhibit a multitude of layers (*12*–*14*). Each is attributed a specific function, which originates mainly in the energies of its frontier molecular orbitals relative to those in all other layers (*15*).

In a typical OLED, the emission layer, where electrons and holes meet to form excitons that radiatively recombine, is sandwiched between a hole- and an electron-injection layer (Fig. 1A). To fulfill the functions that their names imply, the highest occupied molecular orbitals (HOMOs) in the former should ideally lie lower in energy than the HOMOs in the emitter material and, conversely, the lowest unoccupied molecular orbitals (LUMOs) in the latter should lie above the LUMOs in the emitter material. This imposes a driving force for charge carriers of both signs to preferentially accumulate where exciton formation is desired. In addition, the fundamental gaps of the injection layers are chosen to exceed that of the emitting layer so that (i) charges injected from one electrode cannot reach the other and (ii) excitons formed in the emitting layer cannot diffuse to either metallic electrode, where they would recombine nonradiatively.

In the case of a typical OPVC, these two functions are still carried by two outer layers that, however, now serve as hole- and electron-extraction layers, respectively (Fig. 1B). To impose a driving force for selectively collecting photo-generated charges, the HOMOs in the former should lie above those in a donor material in energy and the LUMOs of the latter should lie below those in an acceptor material. Finally, and most importantly, the frontier orbitals in the acceptor must be lower in energy than those in the donor to split bound excitons into free charge carriers at this central interface.

The two generic examples just discussed highlight the critical role of energy-level alignment at organic/organic interfaces. To optimize them, materials choice is often based on the assumption that, upon sequential deposition of one organic-semiconductor layer onto another, the vacuum level (VL), that is, the potential energy of an electron at rest just above the surface, remains constant. This would conveniently imply that, knowing the frontier orbital energies of each material individually, the full energy-level landscape within a multilayer stack could be obtained by simply aligning the HOMO/LUMO levels of all components to that constant VL, as indicated in Fig. 1. As also indicated there, however, a vast body of experimental evidence—often gathered by ultraviolet photoelectron spectroscopy (UPS)—points to the fact that the assumption of VL alignment does not generally hold. On the contrary, interfacial VL shifts in excess of ±1.0 eV are frequently observed (*16*–*19*). These translate into shifts of similar magnitude between the frontier orbital energies of one organic semiconductor relative to the next, thereby compromising the interface functionalities discussed above. Clearly, the underlying reasons for the occurrence (or absence) of these shifts need to be thoroughly understood to enable a truly knowledge-based materials and device design. Despite numerous case studies in literature (*16*–*27*), however, and despite the obvious technological relevance, an explanatory framework that can reliably predict the magnitude, the sign, and the spatial profile of the observed VL shifts at organic/organic interfaces has yet to emerge.

Most existing approaches invoke charge transfer between adjacent organic-semiconductor layers, either between molecules at the very interface, thereby causing an abrupt step in the VL (often termed interface dipole) (*18*, *26*–*29*), or between extended space-charge regions on either side of the interface, leading to more continuous VL shifts (frequently referred to as band bending) (*19*, *20*, *24*, *25*), or both (*16*, *17*, *21*). Any interpretation along these lines naturally entails that, when the layer sequence is reversed, the sign of the VL shift must also be reversed, whereas its absolute value should remain the same. This,

[1]Helmholtz-Zentrum Berlin für Materialien und Energie GmbH, Bereich Solarenergieforschung, Albert-Einstein-Straße 15, 12489 Berlin, Germany. [2]Institut für Physik, Humboldt-Universität zu Berlin, Newtonstraße 15, 12489 Berlin, Germany.
*Corresponding author. E-mail: martin.oehzelt@helmholtz-berlin.de
†Present address: Department of Physics, Faculty of Science and Technology, Tokyo University of Science, 2641 Yamazaki, Noda-city, Chiba 278-8510, Japan.

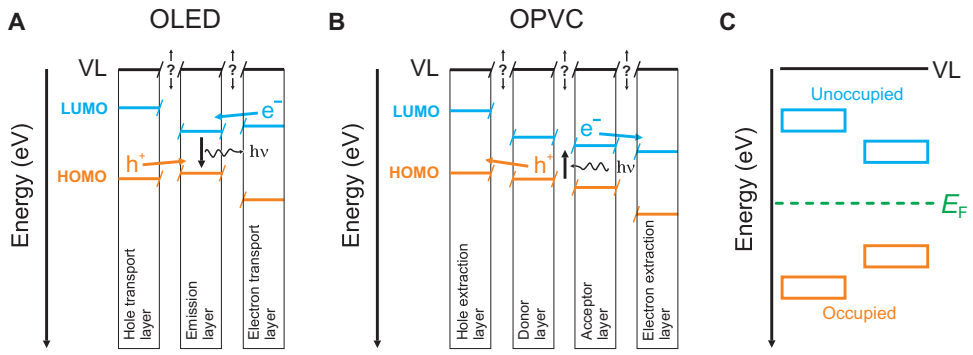

Fig. 1. Schematic representation of multilayer organic optoelectronic devices. (**A**) In a typical OLED, hole (h^+) and electron (e^-) injection layers promote the respective charge carriers to accumulate in the emission layer, where they form excitons, which recombine to emit light (wiggly line labeled *hν*). The desired binding energies of the respective HOMOs and LUMOs are indicated by orange and blue horizontal lines as is the VL in black. The question marks and vertical arrows interrupting the VL highlight that significant interfacial shifts may occur upon contact between organic layers. (**B**) Same for a typical device architecture used in OPVCs. Excitons generated on illumination are separated into free charge carriers at the central organic heterojunctions and selectively extracted by the outer layers. (**C**) Schematic of an organic/organic interface, where VL alignment prevails because the substrate-imposed Fermi level E_F (green) comes to lie well between the occupied (orange) and unoccupied (blue) manifold of electronic states in both semiconductors after mutual contact.

however, is manifestly not always the case (*18*, *19*, *21*, *22*, *25*, *30*). Because even attempts to formulate more generally valid models fail to reproduce band bending entirely (*18*, *22*, *26*, *28*–*30*), a more potent theory is clearly needed to reliably guide the development of next-generation organic (opto-)electronic devices.

Here, we propose such a theory and we apply it to provide a systematic overview of the entire range of achievable energy-level alignment scenarios at organic/organic interfaces. Furthermore, we demonstrate that our model quantitatively reproduces experimental results (notably band bending) in cases where reliable material parameters are available. We hope that the emerging insights will help focus future efforts on custom-tailoring functional organic heterojunctions.

RESULTS AND DISCUSSION

To develop an understanding of such heterojunctions, the first step is to realize that they never occur as free-standing entities in practice, neither in actual devices nor in UPS measurements. In contrast, they are exclusively prepared on conducting substrates, which constitute infinite reservoirs of electrons with constant chemical potential (or Fermi level) E_F. The next important step is to acknowledge that, in any realistic scenario, electronic equilibrium across the entire heterostructure, comprising both organic layers and the substrate, is reached (*22*, *26*, *30*). Denying the possibility for charge equilibration, and thus for the formation of a common E_F (Fig. 1C), would be to deny charge carriers the possibility to move from the substrate through the organic heterostructure. This very possibility, however, lies clearly at the very core of all organic (opto-)electronic devices. Furthermore, the possibility for electrons from the (grounded) substrate to replenish photoholes inevitably created near the surface of the organic heterostructure in the course of a UPS experiment is critical to prevent sample charging, which would preclude obtaining reliable data on the VL and molecular-level shifts that one strives to observe with this method.

Naturally, if E_F comes to lie deep within the fundamental gaps of both organic layers after mutual contact, no or only a negligible amount of charge density will have rearranged within the heterostructure (Fig. 1C). Consequently, the macroscopic electrostatic potential remains unaltered and VL alignment indeed prevails, as often observed (*16*, *17*, *19*, *20*, *22*, *26*). To understand how deviations from VL alignment come about, consider the exemplary scenario in Fig. 2A. It is chosen to represent 10 nm of copper phthalocyanine (CuPc) on 10 nm of aluminum-tris(8-hydroxychinolin)—better known as Alq_3 (see fig. S1A for chemical structures)—on magnesium-covered, tin-doped indium oxide (ITO), because high-quality UPS data are available for this case (*20*). Assuming VL alignment there, E_F ends up well within the fundamental gap of the first organic layer but would come to lie within the LUMO distribution of the second. Presaging the [sometimes acknowledged (*16*–*18*, *20*–*23*, *26*, *30*, *31*) but never rigorously explored] role of the substrate, Fermi-Dirac occupation of all available single-particle states across the entire heterostructure then necessitates that electrons accumulate in the top organic.

Here, to quantify the origin, amount, and spatial profile of these charges as well as the ensuing consequences on VL and frontier orbital energies, we adapt a recently developed model (*32*, *33*), where both organics are discretized into laterally homogeneous sheets and each discretization interval Δz is assigned a material-specific molecular area density, dielectric constant, and density of states (DOS). To limit complexity, we follow the common practice of approximating the energy distribution of both the HOMOs and the LUMOs by a Gaussian (Fig. 2B) (*32*, *34*). For the sake of clarity, however, we will draw only one box each to represent the spatial evolution of the occupied and unoccupied DOS in both materials. The upper and lower edges of these boxes indicate the onsets of the respective Gaussians, which are taken to lie two standard deviations (SDs) above and below their maxima (Fig. 2B).

By occupying the initially VL-aligned organic DOS so constructed up to the E_F dictated by the substrate, a depth-resolved charge-density profile $\rho(z)$ is obtained. Numerically solving the generalized Poisson equation in one dimension yields the corresponding electrostatic potential $V(z)$ within the organic heterostructure. The DOS of each discretization interval is then shifted in energy by the product of electron charge $-e$ and $V(z)$, and is again occupied up to E_F to yield a new $\rho(z)$. This procedure is iterated self-consistently until convergence is reached.

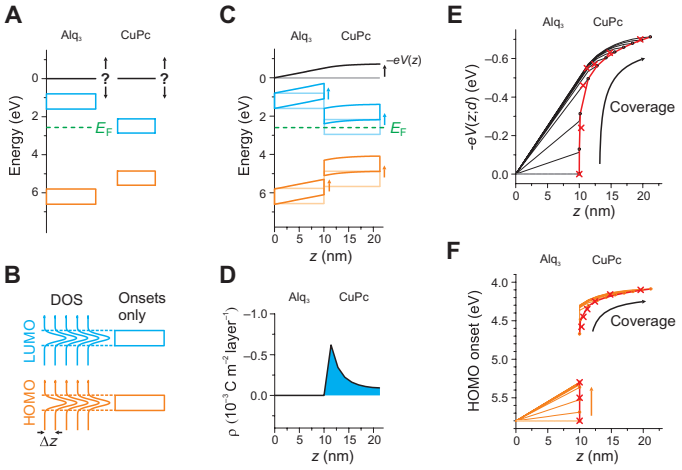

Fig. 2. Exemplary case study of the energy-level alignment at an organic heterojunction. (**A**) Initial situation before deposition of CuPc onto Alq_3, with the Fermi level (E_F = 2.6 eV) indicated by a green dashed line on the binding energy scale. The question mark breaking the VL highlights the possibility for shifts to occur upon completion of the organic heterojunction. (**B**) Schematic illustrating the Gaussian DOS assumed for the energy distributions of the HOMOs and LUMOs in each discretization interval Δ*z* of both organic semiconductors. Throughout the remainder of the manuscript, respective boxes are drawn, with their upper and lower edges indicating the low and high binding energy onsets of these Gaussians, respectively. (**C**) Calculated evolution of the local potential energy, −*eV*(*z*), and HOMO/LUMO distributions in the completed organic heterojunction compared to the initial situation. Vertical arrows highlight respective changes. (**D**) Calculated charge-density (ρ) profile across the completed heterojunction. (**E**) Experimental vacuum-level changes (red crosses) compared to calculated endpoints −*eV*(*d*) for increasing thickness *d* of deposited CuPc (black dots connected with red line). Black lines show the calculated *V*(*z*) for different CuPc thicknesses *d*. (**F**) Experimental HOMO onsets of Alq_3 (bottom) and CuPc (top) upon increasing CuPc coverage (red crosses). Calculated onsets across the entire heterostructure are indicated by orange lines for each CuPc thickness *d*, and the respective endpoints are connected by red lines.

The first striking result (Fig. 2D) is that, in our example, electrons accumulate only in the top organic layer, whereas the bottom layer stays entirely charge-neutral. Therefore, any explanation invoking interfacial charge transfer is evidently inadequate, as is the term "interface dipole." No charge is transferred and no dipole is formed at the organic/organic interface. Rather, the charges in the top layer together with their countercharges in the metallic substrate form a plate capacitor with the bottom organic acting merely as dielectric. This manifests itself in the electrostatic potential (Fig. 2C), which exhibits a linear drop across that bottom layer. In addition, the presence and spatial distribution of electrons in the top layer lead to a noticeable bending of the potential there. Neglecting—for the sake of simplicity—changes to the DOS at the very interface, which can arise from disorder or the inhomogeneous screening of excess charges there (*23*, *35*–*42*), the HOMO/LUMO distributions in each material simply follow the local *V*(*z*), as drawn in Fig. 2C. In contrast to the expectations from simple vacuum-level alignment (Fig. 2A), this leads to E_F lying well between the HOMO and LUMO onsets defining the fundamental gap at the surface of the entire heterostructure. We stress that no additional ingredients are required to obtain this intuitive result, least of all the spontaneous formation of discrete "integer charge transfer states" sometimes invoked in literature (*22*, *26*).

To test the quantitative accuracy of our model and to understand how previous interpretations could have been misled, it is necessary to more closely examine the experimental method that produces the data on which they were based. First, we note that UPS—or Kelvin probe measurements, for that matter (*43*, *44*)—provides information only on the VL directly above the sample surface and not on the local potential *V*(*z*) within the final heterostructure. In an attempt to nevertheless recover *V*(*z*), it is customary to incrementally deposit a second organic semiconductor (CuPc in our case) on top of a first (Alq_3 in our case) and to measure the VL at each thickness *d*. The experimentally obtained series of points *V*(*d*) is shown as red crosses in Fig. 2E (*20*). Comparison with our calculation, shown as a solid red line, reveals excellent agreement. However, our results highlight that the series of endpoints *V*(*d*) accessible by UPS does not match the local potential *V*(*z* < *d*)—shown as black lines—for any thickness. In particular, the steep initial increase of the VL, which could be misinterpreted as arising from an interface dipole, is not reflected in the *V*(*z*) within the final heterostructure.

Moreover, at typically used photon energies of tens of electron volts, UPS is highly surface-sensitive with an information depth restricted to only ~1 to 3 nm (*45*), that is, to the topmost one or two molecular layers. Consequently, only the (occupied) DOS in the topmost layer(s) of the first organic material can be monitored, while the initial layer of the second is deposited. In our example, the shift in the HOMO-derived DOS of Alq_3 observed upon initial CuPc deposition (*20*) is again in near perfect agreement with the shift of the potential in the last Alq_3 layer extracted from our calculations (Fig. 2F). These reveal, however, that the shift is not, in fact, spatially limited to the topmost (and therefore observable) Alq_3 layer(s) but that it is simply a consequence of the DOS following the linear local potential throughout the entire Alq_3 film. Clearly, the assumption that *V*(*z*)—and with it the DOS—remains constant at depths where it can no longer be probed by UPS promotes spurious conclusions (*17*–*20*, *22*, *25*, *27*), such as a space-charge region and band bending in Alq_3 at the interface to CuPc.

Having, on an illustrative example, developed some key points—notably the role of the substrate E_F and the fundamental difference between local potential *V*(*z*) within a heterostructure and the sequence of potentials *V*(*d*) outside a heterostructure—the stage is now set to provide a comprehensive picture of all energy-level alignment scenarios that can be encountered at organic/organic interfaces. To stay as general as possible, we apply our model to a systematic series of heterojunctions made from two organic semiconductors, which are characterized by representative materials parameters differing only in their HOMO and LUMO energies, and are built on substrates with systematically varying E_F.

Type I heterojunctions

Let us start in Fig. 3A with an organic type I heterojunction, relevant for the OLED structure shown in Fig. 1A. In the second panel from the left, the situation just discussed is immediately recognized. Moving on to the central panel, where E_F lies well within the gap of both materials, our model predicts that VL alignment prevails. This is the scenario first introduced in Fig. 1C. Among others, it is observed for the very same CuPc-on-Alq_3 materials combination just discussed when the organic heterojunction is built directly on ITO, where E_F lies

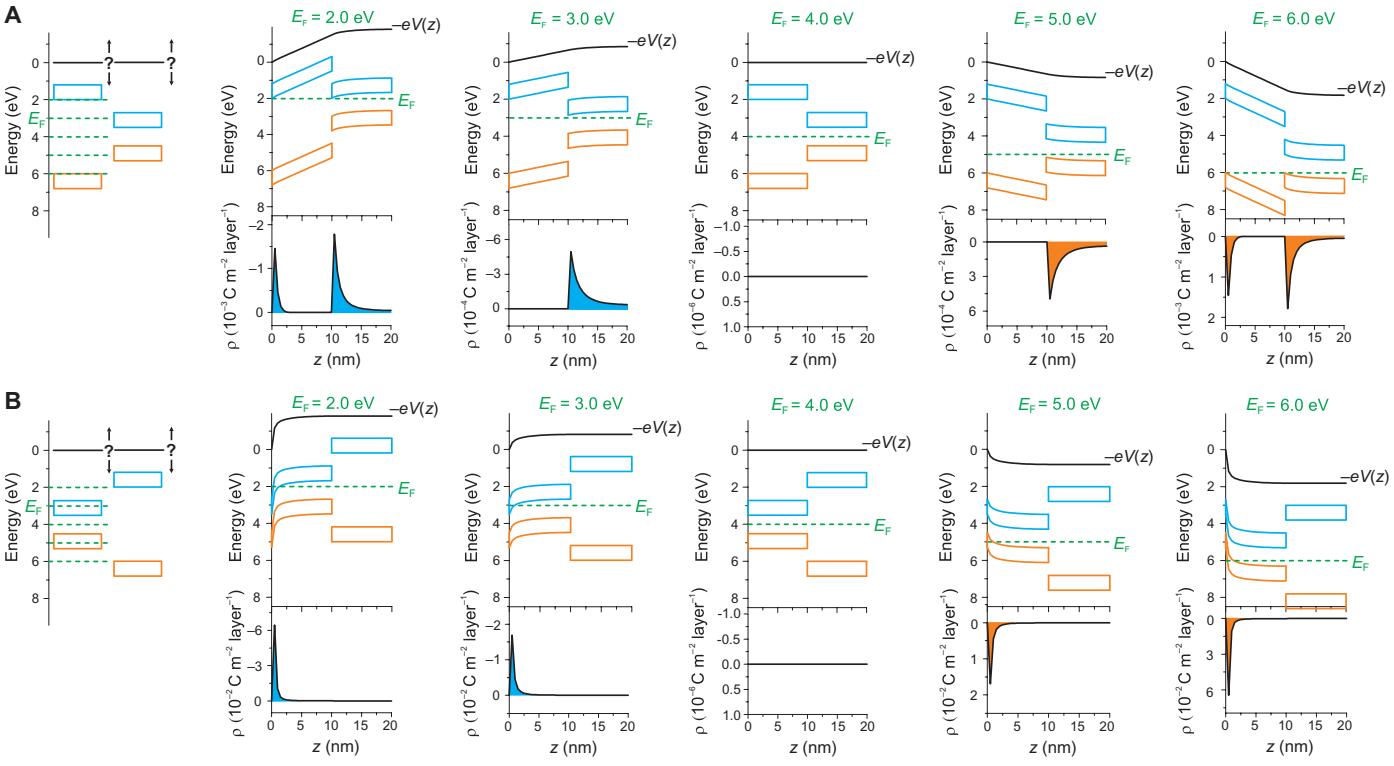

Fig. 3. Numerically calculated energy-level alignment for organic type I heterojunctions. (**A**) The schematic on the very left shows the situation before charge equilibration across the heterostructure and indicates the Fermi-level (E_F) positions for which results are shown in the following five panels. There, the top parts show the spatial evolution of the local potential energy $-eV(z)$ as well as of the HOMO (orange) and LUMO (blue) distributions. The according charge-density (ρ) profiles are shown in the bottom panels, with blue shading indicating electron accumulation in LUMOs and orange shading signifying hole accumulation in HOMOs. (**B**) Same for the reversed stacking sequence. Note that there is, of course, a continuous evolution between the specific scenarios explicitly shown here, but that no qualitatively new cases arise even when the symmetry in the initial energy-level alignment is broken.

deeper below the VL compared to Mg-treated ITO (see fig. S1) (*20*). If E_F is moved further down until it touches the tail of the HOMO distribution in the top organic layer (second panel from the right), the situation is the reverse of that in Fig. 2. The bottom organic again stays charge-neutral but, instead of electrons accumulating in the LUMOs of the top layer, holes are now accumulating in its HOMOs. Consequently, an overall downward shift in the VL (and, with it, the DOS) across the entire heterojunction is now predicted. The fact that all three scenarios—positive, no, and negative VL shifts—can occur for the very same organic materials combination highlights the dominant role of the substrate E_F and questions the viability of attributing the observed phenomena to the organic/organic interface alone (*19*, *24*, *25*, *27*–*29*). For the sake of completeness, we also show in the two outermost panels of Fig. 3A the extreme cases, where E_F already touches the LUMO (left) and HOMO (right) onsets of the bottom (wide-gap) organic semiconductor. In addition to electron/hole accumulation in the top (narrow-gap) organic, charges of the respective sign now also accumulate at the interface to the substrate. It then follows naturally that, if the stacking sequence in a type I heterojunction is reversed (Fig. 3B), charges can accumulate in the bottom (now narrow-gap) organic semiconductor only with no further VL shifts occurring upon deposition of the top (now wide-gap) layer. We note on the side that, whether extended space-charge regions or abrupt interface dipoles are observed at the contact between bottom layer and electrode depends on the nature of that contact and the interfacial organic-semiconductor DOS it entails (*33*, *46*).

Type II heterojunctions

Building upon these results, the OPVC-relevant scenario of an organic type II heterojunction can now be easily understood (Fig. 4A). Starting with the central panel, VL alignment again prevails when E_F lies within the fundamental gap of both organic semiconductors. Because the relative energies of the LUMO distributions are similar to the situation described in Fig. 3A, it is clear that bringing E_F up in energy will result in electrons accumulating first in the top (second panel from the left) and then additionally in the bottom organic layer (leftmost panel) with the VL shifts developing accordingly. Conversely, the HOMO distributions are equivalent to the situation depicted in Fig. 3B. Likewise, hole accumulation and associated VL shifts occur only in the bottom organic if E_F is lowered in energy. For the reverse stacking sequence in a type II heterojunction (Fig. 4B), the correspondence to the scenarios in Fig. 3 is obviously reversed.

Type III heterojunctions

This leaves type III heterojunctions, used, for example, in ambipolar organic field-effect transistors (*47*, *48*), to be discussed (Fig. 5A). Clearly, E_F can no longer lie within the fundamental gaps of both materials in this case. If it lies within the gap of the bottom organic (second panel from left), then it is higher in energy than the entire LUMO distribution in the top layer, which entails electron accumulation and the associated band bending there. The ensuing (linear) potential drop across the bottom layer now lifts the HOMO distribution right at

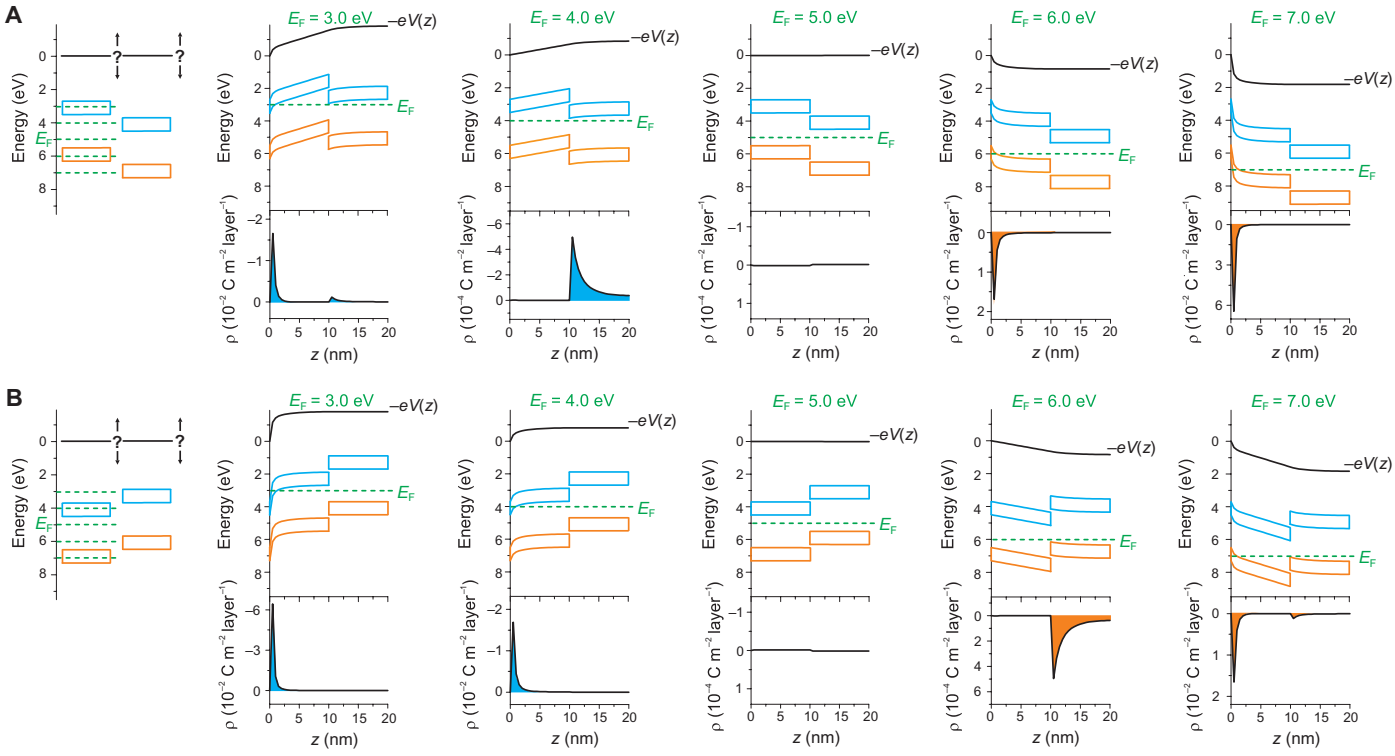

Fig. 4. Numerically calculated energy-level alignment for organic type II heterojunctions. (**A**) The schematic on the very left shows the situation before charge equilibration across the heterostructure and indicates the Fermi-level (E_F) positions for which results are shown in the following five panels. There, the top parts show the spatial evolution of the local potential energy $-eV(z)$ as well as of the HOMO (orange) and LUMO (blue) distributions. The according charge-density (ρ) profiles are shown in the bottom panels, with blue shading indicating electron accumulation in LUMOs and orange shading signifying hole accumulation in HOMOs. (**B**) Same for the reversed stacking sequence. Note that there is, of course, a continuous evolution between the specific scenarios explicitly shown here and in Fig. 3, but that no qualitatively new cases arise even when the band gaps of the two organic semiconductors differ.

the interface to the top layer so far up that its low binding energy tail crosses E_F, leading to electron depletion there. Of all the scenarios considered so far, the overall charge distribution (and the relatively steep local potential step associated with it) is now indeed reminiscent of an interface dipole or, rather, narrow space-charge regions on either side of the heterojunction. This feature persists even when E_F is moved into the LUMO or HOMO manifold of the bottom layer (left and right panels, respectively), which also leads to charge accumulation at its interface to the substrate and, thereby, to more complex potential profiles there. Results for the reversed stacking sequence in the type III case are shown in Fig. 5B and complete an exhaustive list of all possible scenarios encountered at organic/organic interfaces.

A fair number of these scenarios have actually been realized (*16*–*27*), and we applied our model to some of the more intricate cases (see Supplementary Materials) (*19*, *20*, *40*, *49*, *50*). Good overall agreement with experiment underlines that the physical concepts it is based on dominate over potentially occurring additional effects. For example, (true) interface dipoles arising from mutual molecular polarization amount to at most ±0.2 eV (*36*, *37*, *51*) and, therefore, cannot produce the more substantial VL shifts seen, for example, in Fig. 2. If known from atomistic calculations (*36*, *37*, *51*), however, such effects can straightforwardly be incorporated in our model regardless of their magnitude, as can disorder- and/or polarization-induced modifications to the DOS (*23*, *35*–*42*), as well as potentially occurring VL shifts across the substrate/organic interface (*33*, *46*, *52*).

To summarize, we have noted substantial shortcomings in prevalent attempts of predicting the energy-level alignment at organic/organic interfaces and in the interpretation of the experimental data these are based on. Identifying electronic equilibrium with a supporting metallic substrate as key element has allowed us to propose a self-consistent electrostatic model, which, starting from a realistic DOS of two organic semiconductors, relies only on its Fermi-Dirac occupation and the Poisson equation. Encouraged by agreement with experiment, we have used this model to provide a comprehensive overview of all scenarios potentially encountered at organic heterojunctions. The substrate-imposed Fermi level emerges as the central quantity which ultimately determines the sign and the spatial profile of the observable vacuum-level and near-surface molecular-level shifts. These insights now provide a solid basis for the interpretation of past and future experiments. From a theoretical perspective, we envision integration of our model into drift diffusion (*53*–*56*) or kinetic Monte Carlo simulations (*57*–*59*) to explore its implications for device characteristics. Together, such efforts will, ultimately, contribute to the realization of functional heterointerfaces for superior organic (opto-)electronic devices.

MATERIALS AND METHODS

The key components of the numerical model used for the present work are explained in the main text, and further technical details

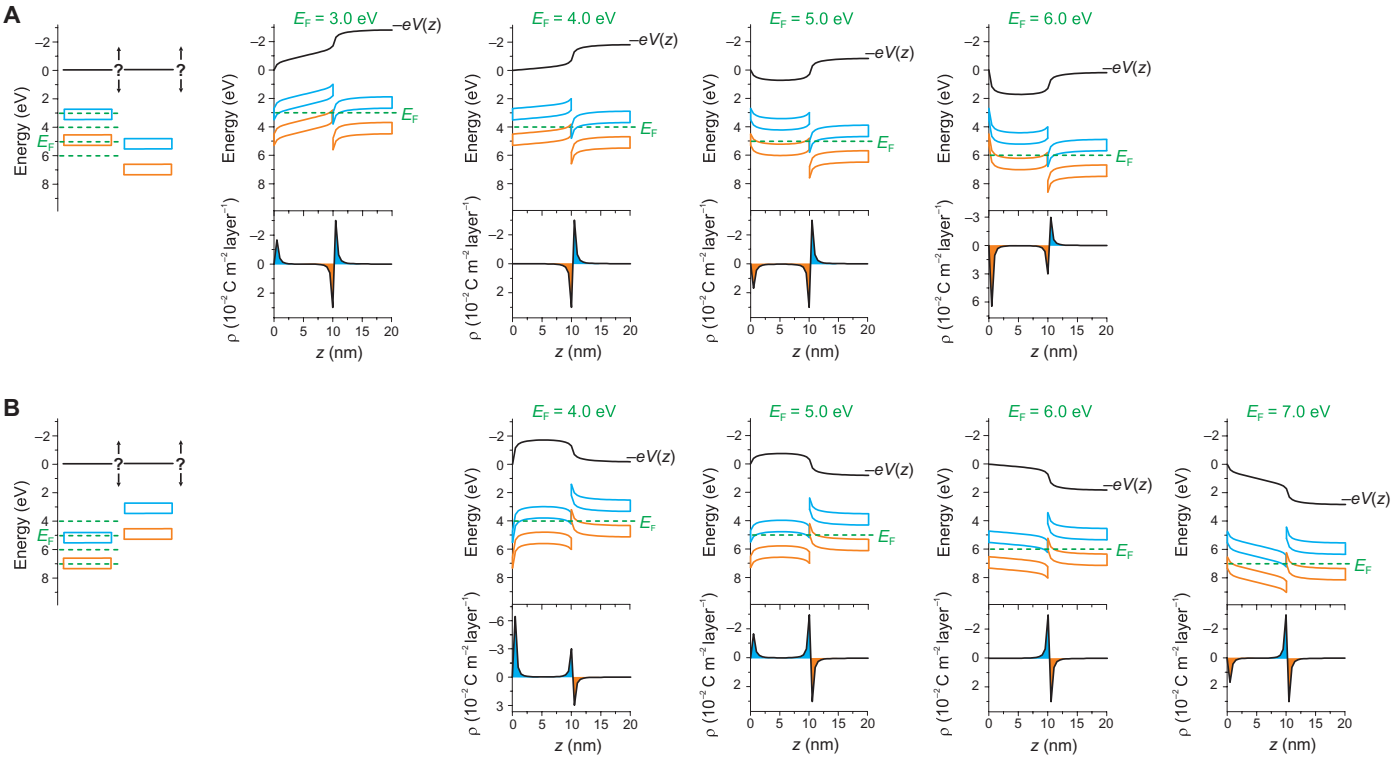

Fig. 5. Numerically calculated energy-level alignment for organic type III heterojunctions. (**A**) The schematic on the very left shows the situation before charge equilibration across the heterostructure and indicates the Fermi-level (E_F) positions for which results are shown in the following four panels. There, the top parts show the spatial evolution of the local potential energy $-eV(z)$ as well as of the HOMO (orange) and LUMO (blue) distributions. The according charge-density (ρ) profiles are shown in the bottom panels, with blue shading indicating electron accumulation in LUMOs and orange shading signifying hole accumulation in HOMOs. (**B**) Same for the reversed stacking sequence. Note that there is, of course, a continuous evolution between the specific scenarios explicitly shown here as well as in Figs. 3 and 4, but that no qualitatively new cases arise even when the band gaps of the two organic semiconductors differ.

are extensively described by Oehzelt *et al.* (*33*). Below, we report the specific materials parameters needed to reproduce the results discussed here, which have all been obtained for a temperature of 300 K.

For Alq_3, the low binding energy onset of the HOMO distribution was extracted as E_{HOMO} = 5.8 eV from Tang *et al.* (*20*), where also the high binding energy onset of the LUMO is given with E_{LUMO} = 1.6 eV. The SD of both the HOMO and the LUMO distributions was taken as $\sigma_{H/L}$ = 0.25 eV, and the respective frontier-orbital (spin-)degeneracies, entering the Fermi-Dirac occupation function (*33*), are both $g_{H/L}$ = 2 for this material. We chose Δz = 1 nm as discretization interval, which yields a molecular area density of $n = 0.9 \times 10^{18}$ m^{-2} according to Suzuki *et al.* (*60*), and assumed a typical dielectric constant of $\varepsilon_r = 4$. The influence of the dielectric constant on the results of the numerical model is rather small. Changing ε_r from 4 to 3 for Alq_3, for example, while retaining all other parameters results in a shift of the final local potential energy in Fig. 2E by only 7 meV, which is well below experimental accuracy and barely visible on the energy scale of Fig. 2E.

For CuPc, assumed to preferentially grow in edge-on orientation, we chose Δz = 1.4 nm, which approximately corresponds to the height of one molecular layer. The well-known bulk crystal structure of this material then yields $n = 2 \times 10^{18}$ m^{-2}. To treat the submonolayer coverages initially deposited onto Alq_3 in Fig. 2, n was reduced accordingly. The values of E_{HOMO} = 4.8 eV, E_{LUMO} = 3.1 eV, and $\sigma_{H/L}$ = 0.25 eV were extracted from Tang *et al.* (*20*); the same $\varepsilon_r = 4$ was assumed but, for CuPc, only g_H = 2, whereas g_L = 4 (*61*).

For the type I scenarios shown in Fig. 3, we used E_{HOMO} = 6.0 eV and E_{LUMO} = 2.0 eV for the prototypical wide-gap organic semiconductor and E_{HOMO} = 4.5 eV and E_{LUMO} = 3.5 eV for the narrow-gap component. For the type II scenarios shown in Fig. 4, the corresponding values were E_{HOMO} = 5.5 eV and E_{LUMO} = 3.5 eV as well as E_{HOMO} = 6.5 eV and E_{LUMO} = 4.5 eV, whereas for the type III cases in Fig. 5, we chose E_{HOMO} = 4.5 eV and E_{LUMO} = 3.5 eV as well as E_{HOMO} = 6.5 eV and E_{LUMO} = 5.5 eV. For all three types of heterojunctions, Δz = 0.5 nm was chosen for both materials components together with the representative parameters $n = 1 \times 10^{18}$ m^{-2}, $\sigma_{H/L}$ = 0.2 eV, $g_{H/L}$ = 2, and ε_r = 4. Note that for zero thickness of the bottom organic layer, the calculated charge density naturally starts with a value of zero (because no molecules are present in that case), as does the electrostatic potential. Consequently, the lines representing the HOMO/LUMO distributions start at the values corresponding to vacuum-level alignment.

SUPPLEMENTARY MATERIALS

Supplementary material for this article is available at http://advances.sciencemag.org/cgi/content/full/1/10/e1501127/DC1

Text

Fig. S1. Exemplary case study of vacuum-level alignment at an organic heterojunction.

Fig. S2. Energy-level alignment for a more complex organic heterojunction.

Fig. S3. Energy-level alignment for reversed deposition sequence.

Fig. S4. Energy-level alignment for an extreme case of a type II heterojunction.

Fig. S5. Energy-level alignment for a type II heterojunction of lying molecules.

References (*62*–*66*)

REFERENCES AND NOTES

1. N. Espinosa, M. Hösel, D. Angmo, F. C. Krebs, Solar cells with one-day energy payback for the factories of the future. *Energy Environ. Sci.* **5**, 5117–5132 (2012).
2. K. A. Mazzio, C. K. Luscombe, The future of organic photovoltaics. *Chem. Soc. Rev.* **44**, 78–90 (2015).
3. K. Knapp, T. Jester, Empirical investigation of the energy payback time for photovoltaic modules. *Sol. Energy* **71**, 165–172 (2001).
4. A. T. Vartanian, I. A. Karpovich, Electric conduction and photoelectric conduction in phthalocyanins. *Doklady Akademii Nauk Sssr* **111**, 561–563 (1956).
5. G. Natta, G. Mazzanti, P. Pino, Hochpolymere von Acetylen-Kohlenwasserstoffen, erhalten mittels Organometall-Komplexen von Zwischenschalenelementen als Katalysatoren. *Angew. Chem. Int. Ed.* **69**, 685–686 (1957).
6. M. Pope, P. Magnante, H. P. Kallmann, Electroluminescence in organic crystals. *J. Chem. Phys.* **38**, 2042–2043 (1963).
7. R. H. Friend, R. W. Gymer, A. B. Holmes, J. H. Burroughes, R. N. Marks, C. Taliani, D. D. C. Bradley, D. A. Dos Santos, J. L. Bredas, M. Logdlund, W. R. Salaneck, Electroluminescence in conjugated polymers. *Nature* **397**, 121–128 (1999).
8. C. W. Tang, A. C. Albrecht, Chlorophyll-a photovoltaic cells. *Nature* **254**, 507–509 (1975).
9. C. W. Tang, S. A. Vanslyke, Organic electroluminescent diodes. *Appl. Phys. Lett.* **51**, 913–915 (1987).
10. C. W. Tang, Two-layer organic photovoltaic cell. *Appl. Phys. Lett.* **48**, 183–185 (1986).
11. C. Adachi, T. Tsutsui, S. Saito, Organic electroluminescent device having a hole conductor as an emitting layer. *Appl. Phys. Lett.* **55**, 1489–1491 (1989).
12. S. M. Menke, W. A. Luhman, R. J. Holmes, Tailored exciton diffusion in organic photovoltaic cells for enhanced power conversion efficiency. *Nat. Mater.* **12**, 152–157 (2013).
13. M. Mesta, M. Carvelli, R. J. de Vries, H. van Eersel, J. J. M. van der Holst, M. Schober, M. Furno, B. Lüssem, K. Leo, P. Loebl, R. Coehoorn, P. A. Bobbert, Molecular-scale simulation of electroluminescence in a multilayer white organic light-emitting diode. *Nat. Mater.* **12**, 652–658 (2013).
14. M. Riede, C. Uhrich, J. Widmer, R. Timmreck, D. Wynands, G. Schwartz, W.-M. Gnehr, D. Hildebrandt, A. Weiss, J. Hwang, S. Sundarraj, P. Erk, M. Pfeiffer, K. Leo, Efficient organic tandem solar cells based on small molecules. *Adv. Funct. Mater.* **21**, 3019–3028 (2011).
15. N. Koch, Organic electronic devices and their functional interfaces. *Chem. Phys. Chem.* **8**, 1438–1455 (2007).
16. S. Zhong, J. Q. Zhong, H. Y. Mao, J. L. Zhang, J. D. Lin, W. Chen, The role of gap states in the energy level alignment at the organic–organic heterojunction interfaces. *Phys. Chem. Chem. Phys.* **14**, 14127–14141 (2012).
17. J. X. Tang, C. S. Lee, S. T. Lee, Electronic structures of organic/organic heterojunctions: From vacuum level alignment to Fermi level pinning. *J. Appl. Phys.* **101**, 064504 (2007).
18. W. Zhao, E. Salomon, Q. Zhang, S. Barlow, S. R. Marder, A. Kahn, Substrate-dependent electronic structure of an organic heterojunction. *Phys. Rev. B* **77**, 165336 (2008).
19. J. Q. Zhong, H. Y. Mao, R. Wang, D. C. Qi, L. Cao, Y. Z. Wang, W. Chen, Effect of gap states on the orientation-dependent energy level alignment at the DIP/F_{16}CuPc donor-acceptor heterojunction interfaces. *J. Phys. Chem. C* **115**, 23922–23928 (2011).
20. J. X. Tang, K. M. Lau, C. S. Lee, S. T. Lee, Substrate effects on the electronic properties of an organic/organic heterojunction. *Appl. Phys. Lett.* **88**, 232103 (2006).
21. Y. Gao, Surface analytical studies of interfaces in organic semiconductor devices. *Mater. Sci. Eng. R* **68**, 39–87 (2010).
22. S. Braun, M. P. de Jong, W. Osikowicz, W. R. Salaneck, Influence of the electrode work function on the energy level alignment at organic-organic interfaces. *Appl. Phys. Lett.* **91**, 202108 (2007).
23. F. Bussolotti, J. Yang, A. Hinderhofer, Y. Huang, W. Chen, S. Kera, A. T. S. Wee, N. Ueno, Origin of the energy level alignment at organic/organic interfaces: The role of structural defects. *Phys. Rev. B* **89**, 115319 (2014).
24. H. Wang, Z. Liu, T. W. Ng, M. F. Lo, C.-S. Lee, D. Yan, S.-T. Lee, Interfacial electronic structure of copper hexadecafluorophthalocyanine and phthalocyanatotin (IV) dichloride studied by photoemission spectroscopy. *Appl. Phys. Lett.* **96**, 173303 (2010).
25. Y. Gao, H. Ding, H. Wang, D. Yan, Electronic structure of interfaces between copper-hexadecafluoro-phthalocyanine and 2,5-bis(4-biphenylyl) bithiophene. *Appl. Phys. Lett.* **91**, 142112 (2007).
26. W. Osikowicz, M. P. de Jong, W. R. Salaneck, Formation of the interfacial dipole at organic-organic interfaces: C-$_{60}$/polymer interfaces. *Adv. Mater.* **19**, 4213–4217 (2007).
27. O. V. Molodtsova, M. Knupfer, Electronic properties of the organic semiconductor interfaces CuPc/C_{60} and C_{60}/CuPc. *J. Appl. Phys.* **99**, 053704 (2006).
28. H. Vázquez, F. Flores, A. Kahn, Induced density of states model for weakly-interacting organic semiconductor interfaces. *Org. Electron.* **8**, 241–248 (2007).
29. H. Vázquez, W. Gao, F. Flores, A. Kahn, Energy level alignment at organic heterojunctions: Role of the charge neutrality level. *Phys. Rev. B* **71**, 041306 (2005).
30. G. Brocks, D. Çakir, M. Bokdam, M. P. de Jong, M. Fahlman, Charge equilibration and potential steps in organic semiconductor multilayers. *Org. Electron.* **13**, 1793–1801 (2012).
31. W. Gao, A. Kahn, Effect of electrical doping on molecular level alignment at organic–organic heterojunctions. *Appl. Phys. Lett.* **82**, 4815–4817 (2003).
32. J. C. Blakesley, N. C. Greenham, Charge transfer at polymer-electrode interfaces: The effect of energetic disorder and thermal injection on band bending and open-circuit voltage. *J. Appl. Phys.* **106**, 034507 (2009).
33. M. Oehzelt, N. Koch, G. Heimel, Organic semiconductor density of states controls the energy level alignment at electrode interfaces. *Nat. Commun.* **5**, 4174 (2014).
34. H. Bassler, Charge transport in disordered organic photoconductors a Monte Carlo simulation study. *Phys. Stat. Sol. B* **175**, 15–56 (1993).
35. S. R. Yost, T. Van Voorhis, Electrostatic effects at organic semiconductor interfaces: A mechanism for "cold" exciton breakup. *J. Phys. Chem. C* **117**, 5617–5625 (2013).
36. S. Verlaak, D. Beljonne, D. Cheyns, C. Rolin, M. Linares, F. Castet, J. Cornil, P. Heremans, Electronic structure and geminate pair energetics at organic–organic interfaces: The case of pentacene/C_{60} heterojunctions. *Adv. Funct. Mater.* **19**, 3809–3814 (2009).
37. N. Sai, R. Gearba, A. Dolocan, J. R. Tritsch, W.-L. Chan, J. R. Chelikowsky, K. Leung, X. Zhu, Understanding the interface dipole of copper phthalocyanine (CuPc)/C_{60}: Theory and experiment. *J. Phys. Chem. Lett.* **3**, 2173–2177 (2012).
38. J. Idé, S. Mothy, A. Savoyant, A. Fritsch, P. Aurel, R. Méreau, L. Ducasse, J. Cornil, D. Beljonne, F. Castet, Interfacial dipole and band bending in model pentacene/C_{60} heterojunctions. *Int. J. Quant. Chem.* **113**, 580–584 (2013).
39. C. Poelking, M. Tietze, C. Elschner, S. Olthof, D. Hertel, B. Baumeier, F. Würthner, K. Meerholz, K. Leo, D. Andrienko, Impact of mesoscale order on open-circuit voltage in organic solar cells. *Nat. Mater.* **14**, 434–439 (2015).
40. K. Akaike, N. Koch, G. Heimel, M. Oehzelt, The impact of disorder on the energy level alignment at molecular donor–acceptor interfaces. *Adv. Mater.* **2** (2015).
41. J. Cornil, S. Verlaak, N. Martinelli, A. Mityashin, Y. Olivier, T. Van Regemorter, G. D'Avino, L. Muccioli, C. Zannoni, F. Castet, D. Beljonne, P. Heremans, Exploring the energy landscape of the charge transport levels in organic semiconductors at the molecular scale. *Acc. Chem. Res.* **46**, 434–443 (2013).
42. G. D'Avino, S. Mothy, L. Muccioli, C. Zannoni, L. Wang, J. Cornil, D. Beljonne, F. Castet, Energetics of electron-hole separation at P3HT/PCBM heterojunctions. *J. Phys. Chem. C* **117**, 12981–12990 (2013).
43. J. K. Arch, S. J. Fonash, Computer simulations of actual and Kelvin-probe-measured potential profiles: Application to amorphous films. *J. Appl. Phys.* **68**, 591–600 (1990).
44. O. M. Ottinger, C. Melzer, H. von Seggern, Pitfalls in Kelvin probe measurements. *J. Appl. Phys.* **106**, 023704 (2009).
45. M. P. Seah, W. A. Dench, Quantitative electron spectroscopy of surfaces: A standard data base for electron inelastic mean free paths in solids. *Surf. Interface Anal.* **1**, 2–11 (1979).
46. H. Wang, P. Amsalem, G. Heimel, I. Salzmann, N. Koch, M. Oehzelt, Band-bending in organic semiconductors: The role of alkali-halide interlayers. *Adv. Mater.* **26**, 925–930 (2014).
47. H. B. Wang, D. H. Yan, Organic heterostructures in organic field-effect transistors. *NPG Asia Mater.* **2**, 69–78 (2010).
48. J. Wang, H. B. Wang, X. J. Yan, H. C. Huang, D. H. Yan, Organic heterojunction and its application for double channel field-effect transistors. *Appl. Phys. Lett.* **87**, 093507 (2005).
49. K. Akaike, N. Koch, M. Oehzelt, Fermi level pinning induced electrostatic fields and band bending at organic heterojunctions. *Appl. Phys. Lett.* **105**, 223303 (2014).
50. W. Chen, D. C. Qi, H. Huang, X. Y. Gao, A. T. S. Wee, Organic–organic heterojunction interfaces: Effect of molecular orientation. *Adv. Funct. Mater.* **21**, 410–424 (2011).
51. J. Beltran, F. Flores, J. Ortega, The role of charge transfer in the energy level alignment at the pentacene/C60 interface. *Phys. Chem. Chem. Phys.* **16**, 4268–4274 (2014).
52. M. T. Greiner, M. G. Helander, W. M. Tang, Z. B. Wang, J. Qiu, Z. H. Lu, Universal energy-level alignment of molecules on metal oxides. *Nat. Mater.* **11**, 76–81 (2012).
53. J. C. Blakesley, D. Neher, Relationship between energetic disorder and open-circuit voltage in bulk heterojunction organic solar cells. *Phys. Rev. B* **84**, 075210 (2011).
54. M. Gruber, B. A. Stickler, G. Trimmel, F. Schürrer, K. Zojer, Impact of energy alignment and morphology on the efficiency in inorganic–organic hybrid solar cells. *Org. Electron.* **11**, 1999–2011 (2010).
55. M. Arar, M. Gruber, M. Edler, W. Haas, F. Hofer, N. Bansal, L. X. Reynolds, S. A. Haque, K. Zojer, G. Trimmel, T. Rath, Influence of morphology and polymer:nanoparticle ratio on device performance of hybrid solar cells—An approach in experiment and simulation. *Nanotechnology* **24**, 484005 (2013).
56. D. Bartesaghi, L. J. A. Koster, The effect of large compositional inhomogeneities on the performance of organic solar cells: A numerical study. *Adv. Funct. Mater.* **25**, 2013–2023 (2015).
57. A. G. Gagorik, J. W. Mohin, T. Kowalewski, G. R. Hutchison, Effects of delocalized charge carriers in organic solar cells: Predicting nanoscale device performance from morphology. *Adv. Funct. Mater.* **25**, 1996–2003 (2015).
58. R. Coehoorn, H. van Eersel, P. Bobbert, R. Janssen, Kinetic Monte Carlo study of the sensitivity of OLED efficiency and lifetime to materials parameters. *Adv. Funct. Mater.* **25**, 2024–2037 (2015).
59. P. Kordt, J. J. M. van der Holst, M. Al Helwi, W. Kowalsky, F. May, A. Badinski, C. Lennartz, D. Andrienko, Modeling of organic light emitting diodes: From molecular to device properties. *Adv. Funct. Mater.* **25**, 1955–1971 (2015).

60. F. Suzuki, T. Fukushima, M. Fukuchi, H. Kaji, Refined structure determination of blue-emitting tris(8-hydroxyquinoline) aluminum(III) (Alq_3) by the combined use of cross-polarization/magic-angle spinning ^{13}C solid-state NMR and first-principles calculation. *J. Phys. Chem. C* **117**, 18809–18817 (2013).
61. N. Marom, O. Hod, G. E. Scuseria, L. Kronik, Electronic structure of copper phthalocyanine: A comparative density functional theory study. *J. Chem. Phys.* **128**, 164107 (2008).
62. W. N. Han, K. Yonezawa, R. Makino, K. Kato, A. Hinderhofer, R. Murdey, R. Shiraishi, H. Yoshida, N. Sato, N. Ueno, S. Kera, Quantitatively identical orientation-dependent ionization energy and electron affinity of diindenoperylene. *Appl. Phys. Lett.* **103**, 253301 (2013).
63. D. G. de Oteyza, E. Barrena, Y. Zhang, T. N. Krauss, A. Turak, A. Vorobiev, H. Dosch, Experimental relation between Stranski–Krastanov growth of DIP/F_{16}CoPC heterostructures and the reconstruction of the organic interface. *J. Phys. Chem. C* **113**, 4234–4239 (2009).
64. A. F. Hebard, R. C. Haddon, R. M. Fleming, A. R. Kortan, Deposition and characterization of fullerene films. *Appl. Phys. Lett.* **59**, 2109–2111 (1991).
65. E. Manousakis, Electronic structure of C_{60} within the tight-binding approximation. *Phys. Rev. B* **44**, 10991–10994 (1991).
66. H. Yoshida, Near-ultraviolet inverse photoemission spectroscopy using ultra-low energy electrons. *Chem. Phys. Lett.* **539**, 180–185 (2012).

Acknowledgments: We thank P. Amsalem and P. Herrmann for fruitful discussions. **Funding:** Financial support through from the Deutsche Forschungsgemeinschaft (DFG) (SFB 951 "HIOS") and the Helmholtz-Energy-Alliance "Hybrid Photovoltaics" is gratefully acknowledged. K.A. acknowledges financial support of the Alexander von Humboldt Foundation. **Author contributions:** M.O. and G.H. devised the model and co-wrote the paper. M.O. implemented the model and performed all calculations. K.A. and N.K. contributed to content discussions and critically commented on the manuscript. **Competing interests:** The authors declare that they have no competing interests. **Data and materials availability:** All data needed to evaluate the conclusions in the paper are present in the paper and/or the Supplementary Materials. Additional data related to this paper may be requested from the authors.

Submitted 18 August 2015
Accepted 18 October 2015
Published 27 November 2015
10.1126/sciadv.1501127

Citation: M. Oehzelt, K. Akaike, N. Koch, G. Heimel, Energy-level alignment at organic heterointerfaces. *Sci. Adv.* **1**, e1501127 (2015).